IOP Publishing Journal of Physics D: Applied Physics
J. Phys. D: Appl. Phys. **46** (2013) 485203 (12pp) doi:10.1088/0022-3727/46/48/485203

Damping Tollmien–Schlichting waves in a boundary layer using plasma actuators

Mark Riherd and Subrata Roy

Applied Physics Research Group, University of Florida, Gainesville, FL 32611, USA

E-mail: roy@ufl.edu

Received 23 August 2013, in final form 25 September 2013
Published 7 November 2013
Online at stacks.iop.org/JPhysD/46/485203

Abstract
The response of a zero pressure gradient boundary layer modified by flow-wise oriented momentum injection similar to that of a plasma actuator is calculated using a two-dimensional (bi-global) stability analysis. It is found that the addition of momentum into the boundary layer has a significant impact on Tollmien–Schlichting waves, which may be damped by up to two orders of magnitude. Changes to the exponential growth rate of the perturbations are also measured. These stabilizing effects are largely due to the momentum addition modifying the downstream boundary layer profiles, but localized stabilization effects are also noted. The relative stabilization of the TS wave appears to be a linear function with respect to the ratio of the plasma-induced wall jet velocity under quiescent conditions and the free-stream velocity for lower levels of plasma actuation (i.e. velocity ratios less than 0.1). For higher levels of plasma actuation, the relative stabilization of the TS wave appears to be exponential with respect to the total momentum addition to the boundary layer by the plasma actuator.

(Some figures may appear in colour only in the online journal)

1. Introduction

Viscous drag is known to be the largest component of drag on ground and air vehicles. For commercial air vehicles, the viscous drag may comprise upwards of 50% of the total drag [1]. On heavy trucks, viscous drag represents 7% of the overall drag on the truck and 26% of the drag on any attached trailers [2]. For high-speed rail, the viscous drag may be up to 70% of the total drag [3]. Economic and environmental benefits can be obtained if the drag experienced by these vehicles is reduced. One approach to reducing the viscous drag is to increase the area of the vehicle wetted by a (low drag) laminar boundary layer, and reduce the area wetted by a (high drag) turbulent boundary layer. Boundary layer stabilization provides a manner of achieving this goal of drag reduction. By stabilizing the boundary layer against external perturbations, a laminar boundary layer can be made less sensitive to the external perturbations that eventually lead to a turbulent boundary layer.

One path of the laminar to turbulent transition process is through the exponentially growing Tollmien–Schlichting (TS) waves [4]. Suppressing the growth of this instability can delay a boundary layer from becoming turbulent. Several different approaches to stabilizing this instability have been examined in the past, including wall suction [5], distributed roughness elements [6], Lorentz force actuators [7], among others.

This study examines the effects of using flow-wise oriented (co-flow) plasma-induced momentum addition to enhance the stability properties of a zero pressure gradient (ZPG) boundary layer flow. In particular, the stability of the boundary layer as it responds to a TS wave generated upstream of a dielectric barrier discharge (DBD) actuator is examined. DBD actuators are devices capable of generating an electrohydrodynamic (EHD) body force, which can be used to add momentum to the nearby fluid [8, 9]. The primary restriction to the use of these actuators is their limited control authority. Under quiescent conditions, most actuator designs are only able to generate wall jet flows up to 3–5 m s^{-1} and produce thrusts per unit length on the order of 20 mN m^{-1}. However, the addition of momentum into the boundary layer suggests that DBD actuators operated in a controlled manner could be very useful for flow stabilization.

For example, Grundmann and Tropea [10, 11] used these actuators for boundary layer stabilization. Operating the actuators in a co-flow orientation with continuous actuation, constantly adding momentum into the boundary layer, they

 © 2013 IOP Publishing Ltd Printed in the UK & the USA

were able to delay the transition by 200 mm for a $10\,\mathrm{m\,s^{-1}}$ flow. Duchmann *et al* [12] made PIV measurements of the TS wave in the region around the plasma actuator, and showed a significant reduction in the wave amplitude and changes to the wave speed relative to the flow without any plasma actuation.

Some theoretical work was also performed describing how momentum addition using EHD devices modifies the boundary layer and its stability properties. For example, flow stabilization downstream of the plasma actuator has been predicted for co-flow oriented momentum addition using local stability analysis and employing boundary layer profiles from experiments [13]. Riherd and Roy performed a local and a limited, preliminary bi-global stability analysis of numerically simulated boundary layers, which also indicated stabilization of the flow [14]. Riherd *et al* have also examined a model of plasma actuated boundary layers, performing very broad parametric studies, identifying a number of trends for the stability of this flow, and tying the gains in stability to the shape factor of the velocity profiles [15].

With regard to specific applications beyond a flat plate, Séraudie *et al* [16] examined the effects of using DBD plasma actuators for the flow over an ONERA-D airfoil at an angle of attack (which generated an adverse pressure gradient over a majority of the chord). Their study employed low-velocity wind tunnel testing (between 7 and $15\,\mathrm{m\,s^{-1}}$) and local stability theory to show the transition delay of the flow. Flight tests using continuous plasma actuation [17] also demonstrated a transition delay of 3% of the chord length for a small aircraft (a G109b motorized glider) for a high Reynolds number flow ($Re_x = \frac{u_\infty x}{\nu} \approx 1.15 \times 10^6$).

This work aims to describe the response of a boundary layer flow modified by plasma actuation to incoming TS waves in terms of the relevant physical mechanisms as well as to quantify the growth and decay rates of perturbations over the length of the boundary layer. Special attention is given to the near-plasma region, including the region where a plasma body force is applied. Furthermore, attention is paid to the linear mechanisms by which the perturbation energy grows or decays. Parametric studies are performed with respect to the amount of plasma actuation, as well as the frequency of the perturbations. A bi-global stability approach is employed to address the two-dimensional base flow where a distributed body force has been applied, which should provide a more robust result than previously employed local stability analysis methods.

This paper is organized as follows. In section 2, the simulation of the boundary layer flows incorporating momentum addition using plasma actuation is described. The flows are then characterized in terms of their boundary layer heights and shape factors, which are relevant to the local stability properties of the boundary layer. In section 3, a linearized bi-global stability approach is described, which is then used to calculate the response of the boundary layer to TS waves generated upstream of the plasma actuator in section 4. From these calculations, the magnitude and exponential growth rates of the TS wave are determined. Based on the magnitudes and growth rates of the TS wave, different spatial domains are identified where the response of the boundary layer to the perturbations is important. The overall damping effect of the plasma-based momentum addition is quantified in terms of the velocity ratio and momentum addition. Finally, appropriate conclusions are drawn in section 5.

2. Determination of the base flow

All types of linear stability analyses require a base flow to examine. As a starting point to examine the effects of plasma-based momentum addition on a ZPG boundary layer, this flow is simulated numerically. This was done using a Navier–Stokes solver, FDL3DI [18], which solves the compressible, diagonalized form of the Navier–Stokes equations in a body fitted coordinate system. Incompressible flows can be solved by setting the Mach number to an appropriately low value. It has been determined that a value of $M_\infty = 0.1$ provides a reasonable balance of incompressibility and numerical stability [18]. Using this Mach number in the present simulations, the maximum variations to the fluid density are found to be on the order of 0.15% throughout the domain, indicating that the flow is essentially incompressible. Temperature (and viscosity via Sutherland's law) variations are similarly small. As such, an incompressible approach to the flow stability should be sufficient.

A fine, two-dimensional mesh (801×151) is used as a domain for the simulation. This domain is non-dimensionalized by the length from the leading edge of the plate to the actuator location. The inlet is located one unit of length upstream of the plate's leading edge and the outlet is seven units of length downstream of the leading edge. This mesh resolves the near-wall boundary layer, effects near a sharp leading edge (but not the leading edge itself) and the steady addition of momentum through a body force term. Far upstream of the leading edge, downstream of the actuator location, and as the mesh approaches the free stream, the mesh is sufficiently coarsened in order to prevent unsteady effects from reflecting off of the boundary conditions. At the location of the plasma actuator ($x = 1$, $Re_x = 100\,000$), 62 points are used to resolve the height of the boundary layer ($\delta_{99\%} = 0.0158$). In total, 45 points are used to resolve the body force in the streamwise direction and 43 points are used to resolve the body force in the wall normal direction. This mesh is quite adequate for resolving the flow details near regions of high gradients, and these simulations should be considered a direct numerical simulation. A schematic of the domain is shown in figure 1. A summary of the dimensional and non-dimensional parameters used for this study is given in table 1.

The plasma actuation is modelled using an approximate body force distribution based on first-principles simulations of the plasma discharge [19] (figure 1(*b*)) in a manner consistent with the description in [18]. While a more rigorous multi-scale analysis may capture the physics of the plasma better, it is anticipated that its response to the flow will not be significantly affected by this approximation or the very high frequency unsteady behaviour ($\mathcal{O}(10\,\mathrm{kHz})$, $F \times 10^6 = \frac{2\pi f \nu}{u_\infty^2} \times 10^6 = \mathcal{O}(10^4)$) that is normally damped out by the boundary layer. Importantly, such an approximation

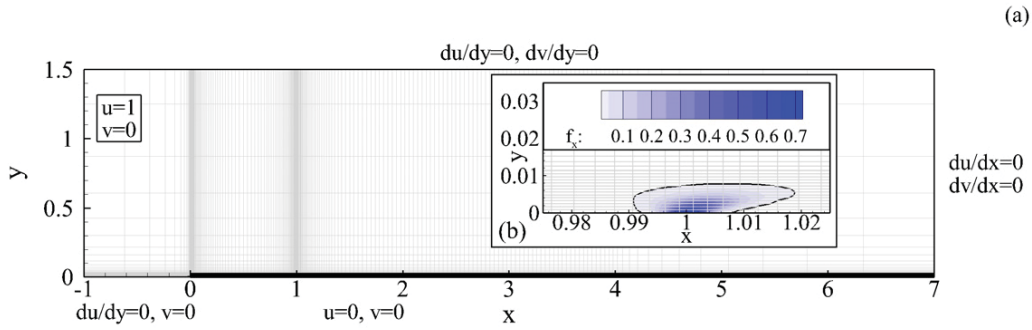

Figure 1. (*a*) Two-dimensional domain and boundary conditions used for the baseline flow modifications, and (*b*) a close up of the co-flow oriented body force used within the boundary layer. Every fourth grid point is shown.

Table 1. Dimensional and non-dimensional values used to compute the base flow.

Reference parameter	Value
Dimensional values	
u_∞	7.5 m s^{-1}
L	0.20 m
ρ_∞	1.20 kg m^{-3}
ν	1.5×10^{-5} m^2 s^{-1}
f	44.7–104.4 Hz
Non-dimensional values	
Re	100 000
Pr	0.72
Ma	0.1
D_c	Varies, see figure 2(*a*)
$F \times 10^6$	75–175

alleviates the expensive computational requirements of a coupled fluid–plasma simulation. The magnitude of the plasma actuation is modulated through a non-dimensional parameter, D_c, which relates the characteristic magnitude of the body force (f_0) to the dynamic pressure (i.e. $D_c = \frac{|f_0|L}{\rho u_\infty^2}$).

Under quiescent conditions, DBD plasma actuators generate a wall jet [8], examples of which are shown in figure 2(*b*). So, instead of defining the magnitude of the body force through a characteristic force density, the magnitude of the body force is characterized by how strong a wall jet it can generate under quiescent conditions, which was determined before simulations of the plasma actuator in a boundary layer. The same setup was used with no-slip conditions ($u = v = 0$) for the left, right and bottom boundaries, with a no-shear condition on the upper boundary, leading to a quiescent condition over a majority of the domain. The body force distribution was operated at various magnitudes of D_c with quiescent initial conditions, representing an increase in the operating voltage of the plasma actuator. As the body force distribution is kept constant for all of the simulations performed as part of this study, the value of D_c is directly proportional to the total amount of body force used to inject momentum into the flow. The effect of the actuation on the flow is then characterized by the maximum velocity induced in the resulting wall jet (u_p, figure 2) at a specific downstream location ($x = 1.03$). An interpolation was then used to control the body force for the simulation under non-quiescent conditions. The magnitude of the implemented force is characterized by the non-dimensional parameter

$$\gamma_0 = \frac{u_p\big|_{x_0,\text{quiescent}}}{u_\infty}. \tag{1}$$

This parameter is selected in order to focus solely on the fluid dynamic effect of the plasma actuation and its influence on the flow stability, ignoring the electrical inputs such as voltage, frequency and the waveform driving the device. The values of γ_0 are calibrated for the Reynolds number tested as part of this study.

Putting this body force into more tangible terms, the total streamwise oriented body force introduced by this model of the distributed force is 2.53×10^{-5} in non-dimensional terms. Using the dimensional parameters laid out in table 1, the total dimensional force per unit width provided to the flow is equal to $0.342 \times D_c$ mN m^{-1}. For the case of $\gamma_0 = 0.25$, $D_c = 12.87$, which results in a total force of 4.40 mN m^{-1}, which is reasonable for generating a 1.88 m s^{-1} wall jet when compared with experimental results [20].

In the simulations, the body force was placed at a position corresponding to a streamwise Reynolds number of $Re_x = 100\,000$ and a displacement boundary layer Reynolds number of $Re_{\delta^*} = \frac{u_\infty \delta^*}{\nu} = 543$ (where $\delta^* = \int_0^\infty (1 - \frac{u}{u_\infty})\,\mathrm{d}y$) in a ZPG boundary layer. This actuator location is in the transitional regime, which is useful for understanding how the momentum addition modifies the laminar to turbulent transition in the critical domain.

In examining the flow fields around the plasma actuator, the addition of momentum can be plainly seen to have a local impact on the boundary layer. The momentum addition region can be seen in the figures (figure 3). Boundary layer profiles are extracted from these flows, and it can be seen that upstream of the plasma actuation, the boundary layer profiles become slightly fuller, due to entrainment effects of the momentum addition. Slightly downstream of the actuator, the boundary layer profiles continue to grow fuller as momentum is injected into the flow, especially in the near-wall region of the boundary layer. The momentum added to the flow quickly diffuses out into the boundary layer, resulting in the velocity profiles farther downstream of the actuator possessing a fuller, more rounded shape. The 'fullness' of the velocity profile is measured by its shape factor ($H = \frac{\delta^*}{\theta}$, where $\theta = \int_0^\infty (\frac{u}{u_\infty})(1 - \frac{u}{u_\infty})\,\mathrm{d}y$),

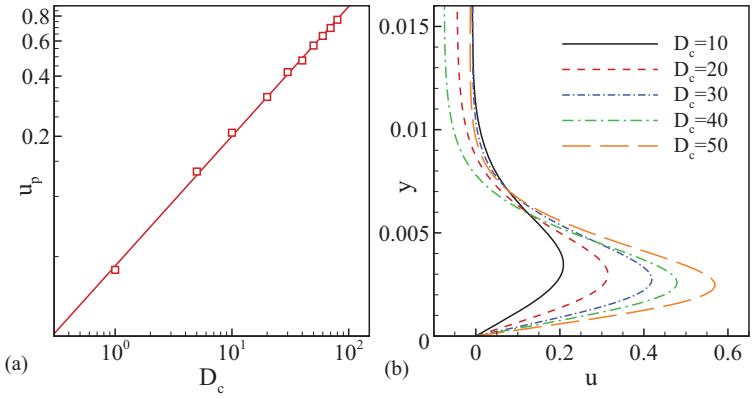

Figure 2. (*a*) Values of u_p used to calibrate D_c. (*b*) Velocity profiles at a location downstream of the plasma actuation for various values of D_c.

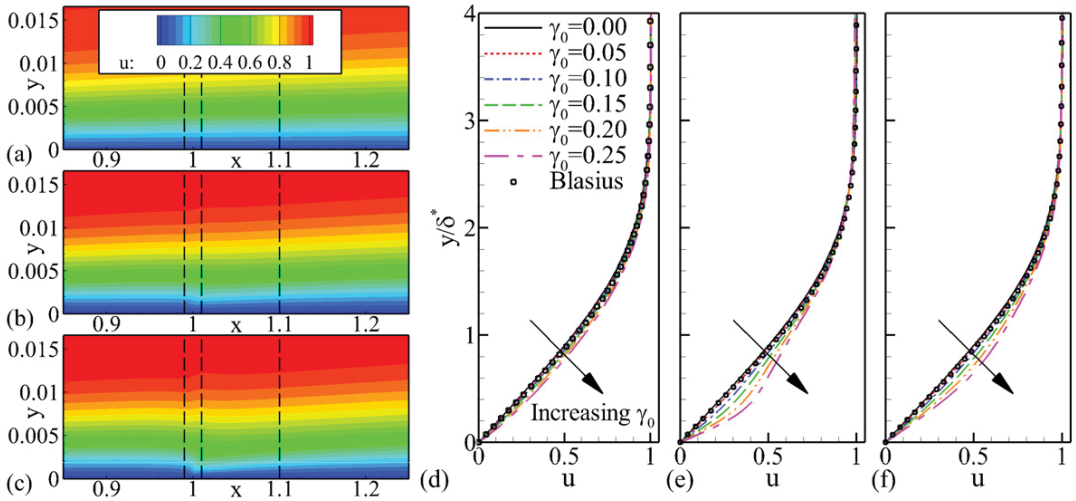

Figure 3. Velocity fields around the plasma actuator for the velocity ratios of (*a*) $\gamma_0 = 0.00$, (*b*) $\gamma_0 = 0.10$ and (*c*) $\gamma_0 = 0.20$. Boundary layer profiles at (*d*) $x = 0.99$, (*e*) $x = 1.01$ and (*f*) $x = 1.10$ are also shown. The dashed lines in (*a*)–(*c*) indicate locations where the boundary layer profiles are extracted from, and are shown in (*d*)–(*f*).

where fuller velocity profiles have smaller values of the shape factor. Changes in the velocity profiles can also be quantified using the shape factor of the boundary layer profiles along the length of the plate (figure 4(*b*)). The reduction in the shape factor from the baseline value of 2.6 indicates that the velocity profiles downstream of the plasma actuators are fuller than those with no actuation applied, and based on the correlation between shape factor and flow stability developed by Wazzan *et al* [21], the flows with actuation should be more stable. The boundary layer heights around the plasma actuator are also modified due to the addition of momentum into the flow. In figure 4(*a*), it can be seen that increased momentum addition results in monotonically larger changes to the displacement boundary layer heights.

Examining where the changes to the boundary layer profiles occur (figure 4), it can be seen that the changes are primarily local, though the boundary layer heights are slightly modified downstream of the actuator location. As such, three different spatial regions can be identified in the flow with respect to the changes in the boundary layer heights. The first of these regions is the region upstream of the actuator (I), where the changes to the flow are minimal. Of the effects that can occur, the flow immediately upstream of the actuator may be slightly stabilized due to fluid being entrained closer to the surface by the body force. The second region is the area that is directly around the plasma actuator (II). In this region, the changes to the boundary layer heights and velocity profiles are the most profound, and the largest gains in stability control should be realized in this area. The final region of the flow is farther downstream of the actuator (III), where the boundary layer flow has largely relaxed back to that of a ZPG boundary layer. However, in this region the boundary layer heights are reduced by a few per cent, due to the addition of momentum into the boundary layer by the plasma actuator.

3. Numerical method

3.1. Bi-global stability approach

In order to determine the response of the plasma-modified boundary layer to oncoming TS waves, a bi-global stability

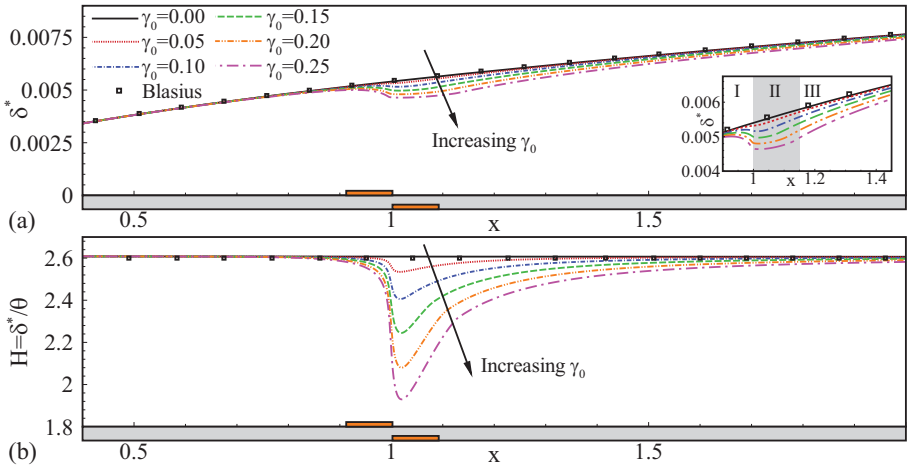

Figure 4. (*a*) δ^* and (*b*) the shape factor as a function of the velocity ratio, γ, for values ranging from 0 to 0.25, with a spacing of 0.05. The inset figure shows a zoomed-in view near the actuator location with the three characteristic zones shown. The size of the actuator is also exaggerated in order to be more visible.

approach is employed. The velocity field, u, and pressure field, p, can be decomposed into the steady equilibrium and perturbation components, where $u_i = \bar{u}_i + u_i'$ and $p = \bar{p} + p'$. Using this decomposition, the incompressible Navier–Stokes equations can be linearized around this steady point such that

$$\frac{\partial u_i'}{\partial x_i} = 0 \tag{2a}$$

$$\frac{\partial u_i'}{\partial t} + \bar{u}_j \frac{\partial u_i'}{\partial x_j} + u_j' \frac{\partial \bar{u}_i}{\partial x_j} + \frac{\partial p'}{\partial x_i} - \frac{1}{Re} \frac{\partial^2 u_i'}{\partial x_j^2} = 0. \tag{2b}$$

Assuming that these perturbations are periodic in time, such that $u_i' = \tilde{u}_i \exp(-\mathrm{i}\omega t)$, the problem can be put into a matrix operator form such that

$$\mathrm{i}\omega \boldsymbol{B}\boldsymbol{u} = \boldsymbol{A}\boldsymbol{u} + \boldsymbol{f} \tag{3}$$

where

$$\boldsymbol{u} = \begin{bmatrix} \tilde{u} \\ \tilde{v} \\ \tilde{p} \end{bmatrix}, \quad \boldsymbol{A} = \begin{bmatrix} \frac{\partial(\cdot)}{\partial x} & \frac{\partial(\cdot)}{\partial y} & 0 \\ \mathcal{C} - \mathcal{D} + \frac{\partial \bar{u}}{\partial x} & \frac{\partial \bar{u}}{\partial y} & \frac{\partial(\cdot)}{\partial x} \\ \frac{\partial \bar{v}}{\partial x} & \mathcal{C} - \mathcal{D} + \frac{\partial \bar{v}}{\partial y} & \frac{\partial(\cdot)}{\partial y} \end{bmatrix},$$

$$\boldsymbol{B} = \begin{bmatrix} 0 & 0 & 0 \\ I & 0 & 0 \\ 0 & I & 0 \end{bmatrix}. \tag{4}$$

The convection and viscous diffusion operators $\mathcal{C}$ and $\mathcal{D}$ are defined as $\mathcal{C} = \bar{u}\frac{\partial(\cdot)}{\partial x} + \bar{v}\frac{\partial(\cdot)}{\partial y}$ and $\mathcal{D} = \frac{1}{Re}(\frac{\partial^2(\cdot)}{\partial y^2} + \frac{\partial^2(\cdot)}{\partial y^2})$. $\boldsymbol{f}$ indicates a periodic forcing to the system. $\boldsymbol{u}$ represents the system's response to that force. Both $\boldsymbol{f}$ and $\boldsymbol{u}$ are complex vectors with real and imaginary parts. The response of the system can be evaluated by solving the system of equations shown above such that

$$\boldsymbol{u} = [\mathrm{i}\omega \boldsymbol{B} - \boldsymbol{A}]^{-1} \boldsymbol{f}. \tag{5}$$

For the present case the periodic forcing term $\boldsymbol{f}$ represents a non-homogeneous boundary condition at the inlet of the domain. Only two-dimensional TS waves are examined as part of this study, as Squire's theorem predicts that two-dimensional TS waves grow more quickly than three-dimensional TS waves [22]. However, we do not discount the fact that three-dimensional instability mechanisms, such as boundary layer streaks [23, 24], can also lead to turbulent flow. Those three-dimensional instabilities are beyond the scope of this work, but are a topic of future research.

3.2. Numerical discretization and boundary conditions

In order to perform these calculations, the matrix operations described in equations (2*a*)–(4) are discretized on a semi-staggered mesh. A subdomain of the velocity fields and their gradients simulated in section 2 ($0.52 \leqslant x \leqslant 4.69$, $0 \leqslant y \leqslant 0.157$) were interpolated onto this mesh. By limiting the domain of the stability analysis to only the boundary layer, receptivity issues at the leading edge of the plate can be neglected, as well as any receptivity issues regarding how the initial TS waves are produced from acoustic or vortical disturbances. The momentum equations are solved and velocity data are stored on a set of points coincident with the domain boundaries. The continuity equation is solved and pressure data are stored on the intermediate set of points. For the differencing, Chebyshev collocation methods are used in the y-direction. In the x-direction, fourth-order accurate centred differencing is used for a majority of the domain. The exception to this is the streamwise convection term, $\bar{u}\frac{\partial(\cdot)}{\partial x}$. This term is up-winded using a third-order accurate finite difference stencil. Next to the boundaries, lower order stencils are used.

For boundary conditions, a TS wave is enforced at the inlet to the domain by way of the vector $\boldsymbol{f}$ (equation (3)), examples of which are shown in figure 5. These TS waves are calculated using a local, spatial eigenvalue solver. The shape of the incoming TS wave is varied depending on the perturbation frequency. For the boundary layer wall and the free-stream, no-slip conditions are employed. In the latter portion of the domain, a sponge region is implemented in order to damp

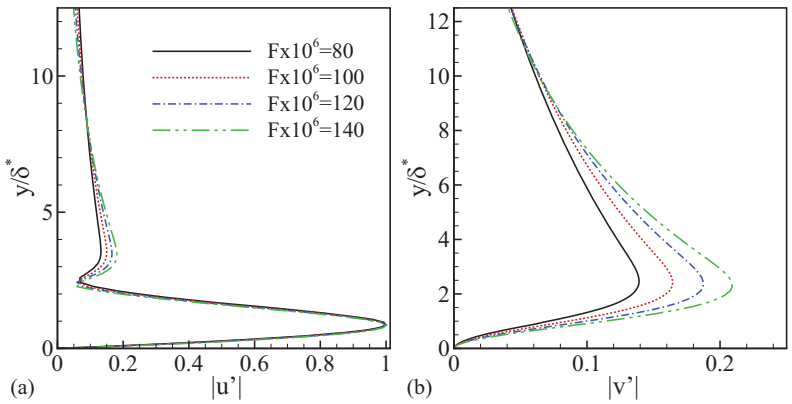

Figure 5. A sample of the (*a*) *u* and (*b*) *v* velocity component perturbations enforced at the inlet of the domain at varying frequencies.

Table 2. Details of the grid resolution study performed. The Very Fine-L, Fine-H, and Tall cases are identical.

Study	Case	N_x	N_y	L_x/δ_0^*	L_y/δ_0^*	$\Delta x/\delta_0^*$	$\Delta y_{\text{wall}}/\delta_0^*$
Streamwise resolution	Coarse-L	513	65	1061.7	40	2.0736	0.02409
	Medium-L	725	65	1061.7	40	1.4664	0.02409
	Fine-L	1025	65	1061.7	40	1.0368	0.02409
	VeryFine-L	1449	65	1061.7	40	0.7332	0.02409
Wallnormalresolution	Coarse-H	1449	33	1061.7	40	0.7332	0.09631
	Medium-H	1449	49	1061.7	40	0.7332	0.04282
	Fine-H	1449	65	1061.7	40	0.7332	0.02409
Height	Short	1449	33	1061.7	20	0.7332	0.04815
	Medium	1449	49	1061.7	30	0.7332	0.03212
	Tall	1449	65	1061.7	40	0.7332	0.02409

out the velocity perturbations as they approach the outlet. This sponge region effectively prevents the perturbations from reflecting off of the outlet and affecting the upstream flow.

3.3. Grid resolution study

A grid resolution study was performed in order to ensure that the problem is adequately resolved. Details of the domain and mesh parameters are indicated in table 2. This study was performed on the unforced boundary layer, but addition grid resolution studies for boundary layers where momentum addition was applied were also performed, indicating similar convergence. Those results are not shown for brevity.

In order to quantify the growth and decay of the TS wave as it propagates downstream, the magnitude of the perturbations along a line in the flow is measured, a sample of the results can be seen in figure 6(*a*). Examining the convergence of the results as a function of the streamwise grid density, it can be seen in figure 6(*c*) that the results approach convergence as the mesh density increases.

Comparing the spatial exponential growth rates of these perturbations (figure 6(*b*)), it can be seen that there is good agreement between the different meshes using this bi-global method. Comparisons can also be made with local stability methods, which predict similar behaviour, though the exact values differ by a small amount. In order to make a good comparison with the bi-global stability analysis, the local growth rates are normalized by the local boundary layer displacement height and multiplied by a factor of two to account for the energy (rather than velocity) perturbation growth. Convergence studies for the wall normal mesh density (figure 6(*d*)) and domain height (figure 6(*e*)) are also examined, and show good convergence.

Based on this grid resolution study, all computations will be performed using the Very Fine-L mesh, and the magnitude of the boundary layer perturbations is assumed to be accurate to within a few per cent.

4. Results

By comparing the instantaneous perturbation flow fields (figure 7), it can be seen that as the magnitude of the plasma actuation is increased, the perturbations are increasingly damped downstream of the plasma actuator.

The metric

$$A_u(x) = \frac{\int_0^\infty \left(|u'|^2 + |v'|^2\right) \mathrm{d}y\Big|_x}{\int_0^\infty \left(|u'|^2 + |v'|^2\right) \mathrm{d}y\Big|_{x=\text{inlet}}} \tag{6}$$

is used to quantify the magnitude of the boundary layer perturbation. This metric quantifies the amount of kinetic energy in the flow along a given point in x.

By applying this metric, the magnitudes of the perturbations are calculated, samples of which can be seen in figure 8 for several different forcing frequencies. In examining the magnitudes of these perturbations, the amount of damping caused by the addition of flow-wise momentum

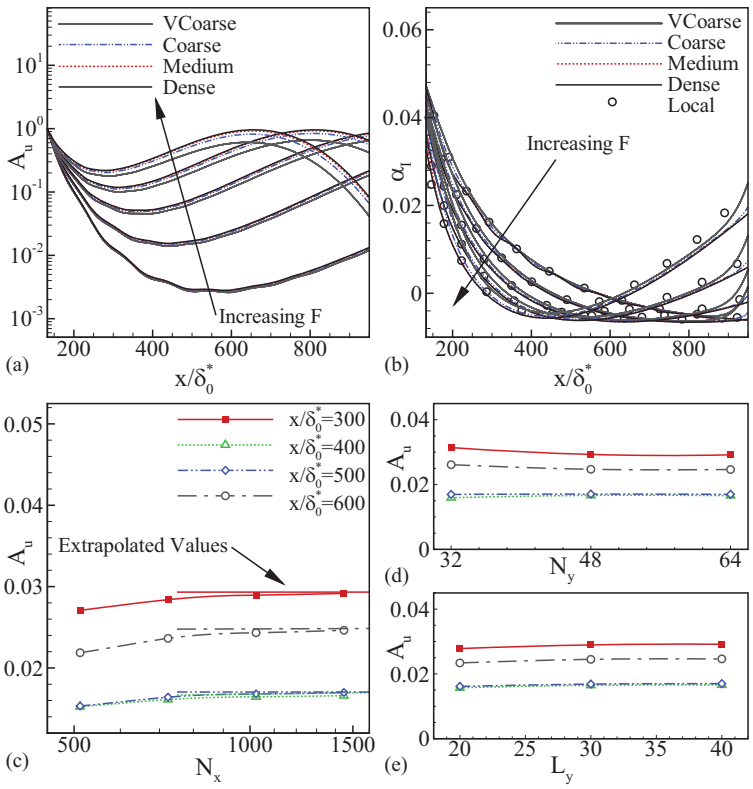

Figure 6. Comparison of the (*a*) amplitudes and (*b*) spatial growth rates of the incoming TS waves for different mesh densities for five different frequencies. These metrics are defined in equations (6) and (7). The convergence of the $F \times 10^6 = 150$ case can also be seen for the (*c*) streamwise grid resolution, (*d*) wall normal grid resolution and (*e*) height of the domain.

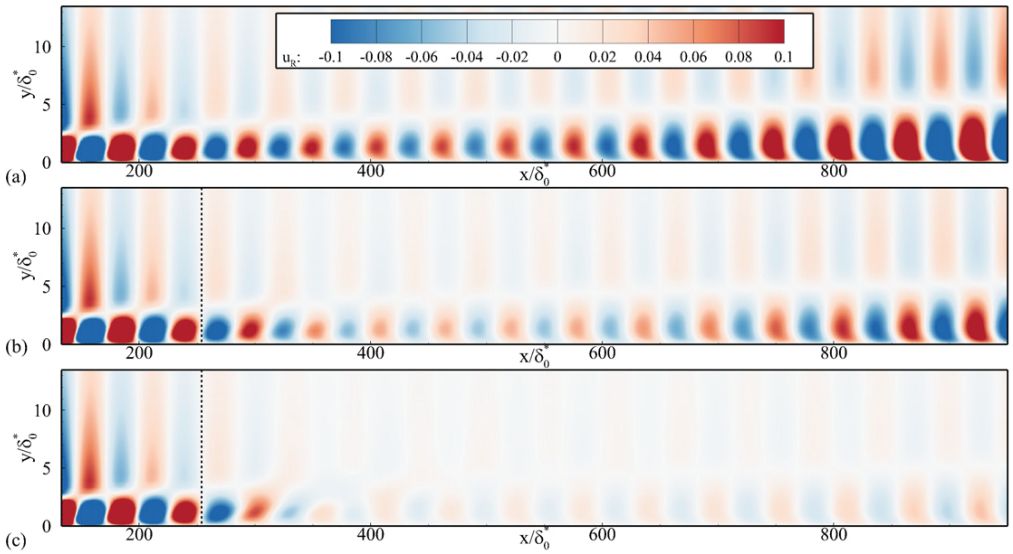

Figure 7. Real component of the u' perturbation velocity for the non-dimensional frequency of $F \times 10^6 = 100$ and plasma actuation levels of (*a*) $\gamma_0 = 0.00$ (no plasma actuation), (*b*) $\gamma_0 = 0.10$ and (*c*) $\gamma_0 = 0.20$. The dashed line indicates the location of the plasma actuator. The contour values in this plot do saturate for $-0.1 < u_r$ and $0.1 > u_r$ in order to show greater detail for smaller values of the perturbation velocity.

into the boundary layer is found to be significant. As the velocity ratio of the plasma actuation is increased, the magnitude of the energy perturbations is decreased by up to two orders of magnitude (only a single order of magnitude for the velocity perturbations). In terms of N-factor, the damping of these perturbations is equivalent to a drop in the N-factor of approximately 2.3 relative to the non-actuated case. Considering that a transition is normally assumed to occur in

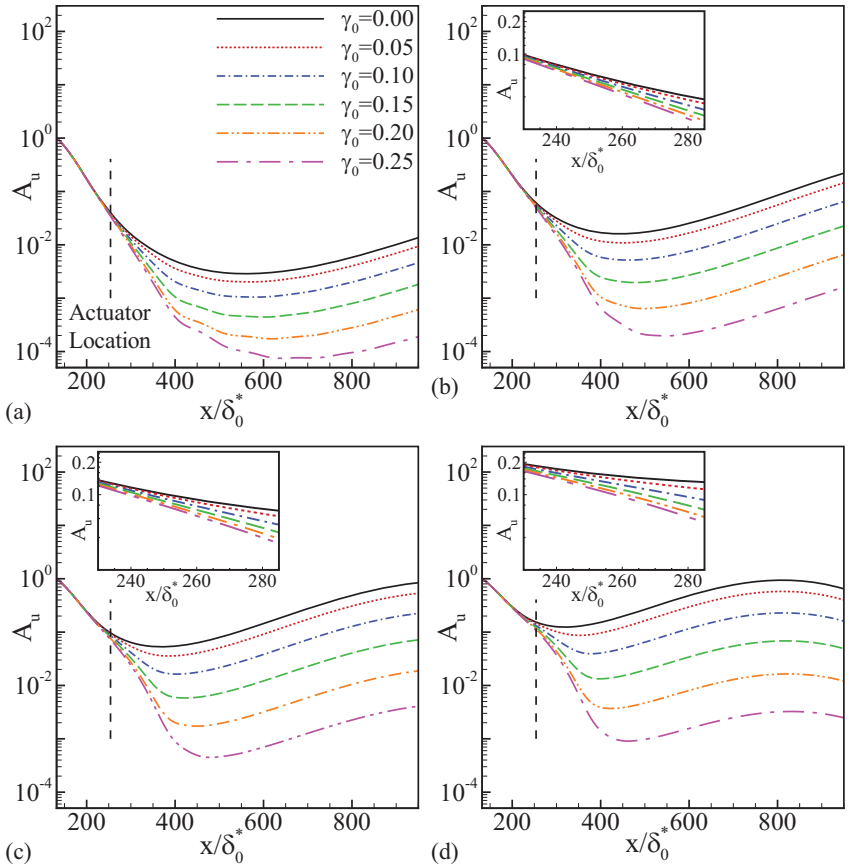

Figure 8. Magnitude of the perturbations as measured using the metric A_u for the non-dimensional frequencies (*a*) $F \times 10^6 = 80$, (*b*) $F \times 10^6 = 100$, (*c*) $F \times 10^6 = 120$ and (*d*) $F \times 10^6 = 140$. The vertical dashed line indicates the location of the actuator, and the inset figures are a close up of the near-actuator region.

a boundary layer for an N-factor of 9–10 [25], this damping of the perturbation could delay the transition by a significant amount.

Based on these data, the growth rates of these perturbations can be calculated. The exponential growth rate is defined as

$$\alpha_I = -\frac{1}{A_u}\frac{\mathrm{d}A_u}{\mathrm{d}x}. \tag{7}$$

The growth rates for a number of cases are shown in figure 9 for several different forcing frequencies. For these calculations, a negative value of α_I indicates instability (perturbation growth), while a positive value of α_I indicates stability (perturbation decay).

By examining the flow fields, perturbation magnitudes and exponential growth rates, it can be seen that the behaviour of the TS wave is not homogeneous along the length of the boundary layer when plasma actuation is introduced into the boundary layer. Rather, there appear to be a number of distinct regions in the flow where this behaviour changes. These regions can be described as the region upstream of the actuator, the regions immediately around and downstream of the actuator where the momentum addition by the body force strongly modifies the flow field, and finally the region sufficiently far downstream such that the modifications to the boundary layer have relaxed enough to become negligible.

The first region in the flow is the region upstream of the actuator ($x/\delta_0^* < 240$), which exhibits only weak changes in its response to perturbations at the domain inlet. In this region, the behaviour of the flow is slightly stabilized with the addition of plasma actuation relative to the non-actuated case, but there are no significant changes to the structure of the TS wave.

A second region in the flow can be defined as the region directly around the plasma actuator and its body force ($240 < x/\delta_0^* < 260$). Around the actuator, the TS wave rapidly begins to decay in magnitude (figure 8, inset) to a lower value than it possessed upstream of the device. As the disturbance moves over the body force region, production of the wave's kinetic energy (defined here using the turbulent kinetic energy production, $P = -\overline{u_i' u_j'}\frac{\partial \overline{u}_i}{\partial x_j}$) is reduced, and even becomes negative for large enough amounts of plasma actuation (figures 10(*b*), (*e*) and (*h*)). Kinetic energy production is normally offset by dissipation (defined here using the turbulent kinetic energy dissipation, $\epsilon = \frac{2}{Re}\overline{s_{ij}' s_{ij}'}$ where $s_{ij}' = \frac{1}{2}(\frac{\partial u_i'}{\partial x_j} + \frac{\partial u_j'}{\partial x_i})$, figures 10(*c*), (*f*) and (*i*)). In the present scenario, the production of the TS wave's kinetic energy is reversed by the addition of the body force, which immediately begins to attenuate the perturbation magnitude, with dissipative effects compounding this attenuation. This near immediate drop in perturbation's growth around the plasma actuator

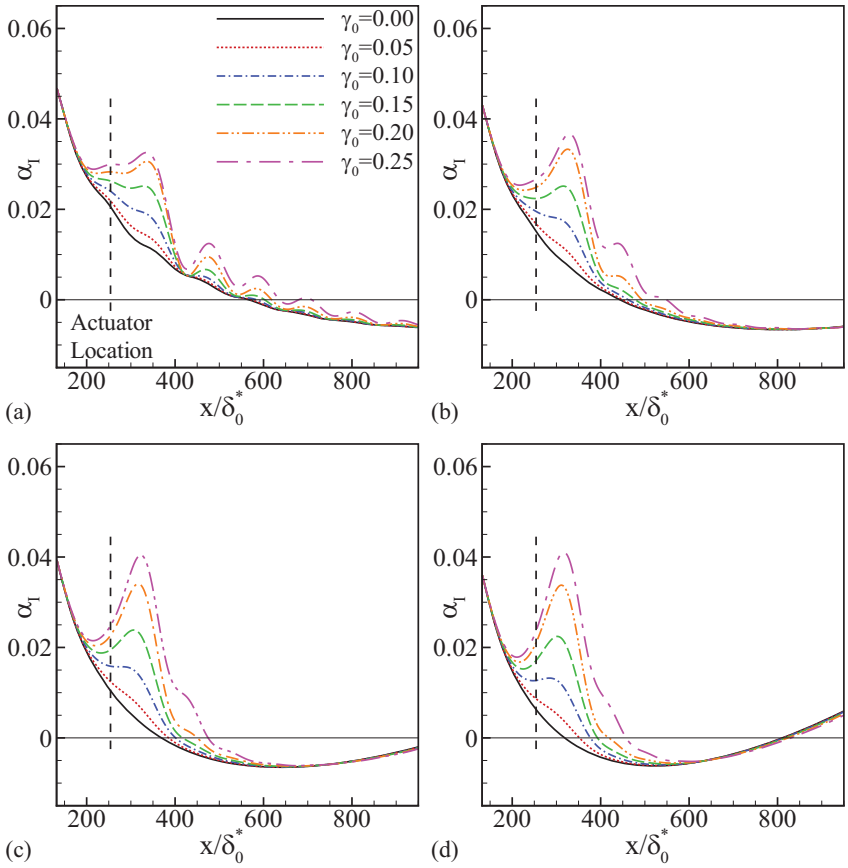

Figure 9. Exponential growth rates of the perturbations for the non-dimensional frequencies (*a*) $F \times 10^6 = 80$, (*b*) $F \times 10^6 = 100$, (*c*) $F \times 10^6 = 120$ and (*d*) $F \times 10^6 = 140$.

indicates that the localized changes in the velocity field around the body force region are stabilizing. Again, there is no significant change in the structure of the TS wave at this point (figure 11(*a*)), even though its magnitude does begin to drop at this point.

By examining the flow fields downstream of the actuator ($260 < x/\delta_0^* < 600$, shown in figure 10), it is seen that the effects of flow stabilization continue (figure 10). The reduced production of perturbation kinetic energy leads to additional attenuation of the TS wave. The amount of perturbation energy production and dissipation are reduced in the flow farther downstream of the actuator, though this can likely be attributed to the reduced magnitude of the TS wave in this region. Furthermore, it seems that as soon as the wave convects over the actuator, it moves slightly away from the wall, before moving back down towards it. This effect is very small for the weaker levels of plasma actuation, but can be more clearly seen for $\gamma_0 = 0.20$ and $\gamma_0 = 0.25$. This movement of the TS wave away from the wall can be more clearly seen through the perturbation velocity profiles (figure 11). It can be seen that the TS waves are modified by the changing boundary layer profiles, but in the near-actuator region, the shape of the TS wave is preserved. However, as one examines the velocity profiles farther downstream where the perturbation has moved away from the wall, the shape of the perturbation changes significantly for the cases involving higher levels of plasma actuation, and more of the perturbation's energy is transferred away from the wall (i.e. $\gamma_0 = 0.20$ and $\gamma_0 = 0.25$).

As the modifications to the boundary layer by the body force relax back to zero as one moves downstream, the TS wave eventually returns to its original state. It can be seen in the perturbation growth rates (figure 9), that the growth of the perturbations matches the baseline non-actuated case downstream of the plasma actuator, indicating that this final region begins at $x/\delta_0^* \approx 600$. Beyond this point, it would seem that the impact of the momentum addition is essentially zero.

4.1. Overall stabilization of the TS wave

Understanding the localized behaviour of the flow stabilization provides insight into the underlying physical mechanisms at play, but at the same time, it is also beneficial to reduce the entire TS wave stabilization process down to a single value, such that the total effect of the stabilization can be understood. In order to understand this total effect of the addition of momentum into the boundary layer using DBD plasma actuation, the ratio of the perturbation magnitudes with and without plasma actuation can be used. In figure 12(*a*), it can be seen that sufficiently far downstream of the plasma actuation (i.e. the region where the modifications to the stability properties have relaxed away), the ratio of the perturbation

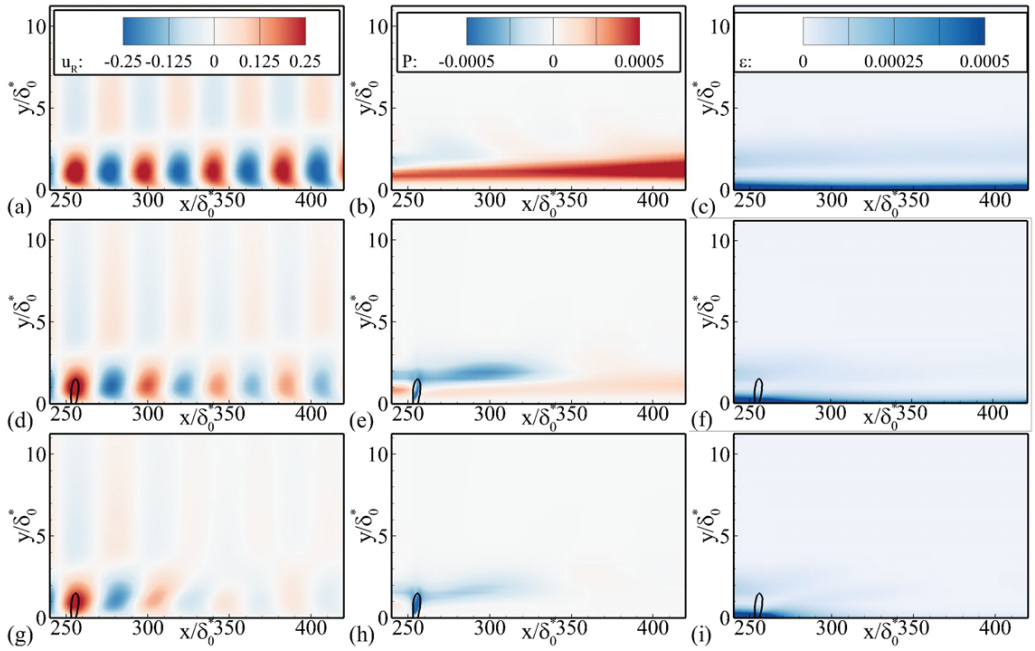

Figure 10. (*a*), (*d*), (*g*) Real component of the *u* perturbation velocity for the non-dimensional frequency of $F \times 10^6 = 140$, (*b*), (*e*), (*h*) perturbation kinetic energy production and (*c*), (*f*), (*i*) perturbation kinetic energy dissipation for plasma actuation levels of (*a*)–(*c*) $\gamma_0 = 0.00$ (no plasma actuation), (*d*)–(*f*) $\gamma_0 = 0.10$ and (*g*)–(*i*) $\gamma_0 = 0.20$. The black line indicates a domain within which the body force is at least 10% of its maximum. The contour values in this plot saturate in order to show greater details for smaller values of the perturbation velocity, perturbation kinetic energy production and perturbation kinetic energy dissipation.

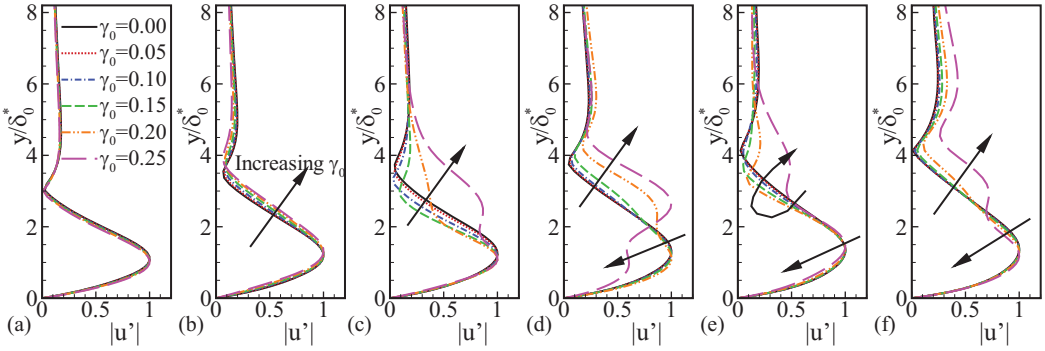

Figure 11. u-velocity profiles of the boundary layer disturbance at selected points in the boundary layer, normalized by each profile's maximum value for $F \times 10^6 = 100$. (*a*) $x/\delta_0^* = 250$, (*b*) $x/\delta_0^* = 300$, (*c*) $x/\delta_0^* = 350$, (*d*) $x/\delta_0^* = 400$, (*e*) $x/\delta_0^* = 400$, and (*f*) $x/\delta_0^* = 450$.

magnitudes is approximately constant. An average of the ratio of the perturbation magnitudes can be taken over a length of the boundary layer downstream of the actuation (B_u) in order to quantify this ratio in a more general manner. Defining this metric as

$$B_u = \frac{1}{x_e - x_s} \int_{x_s}^{x_e} \frac{A_u\,(x, \gamma_0)}{A_u\,(x, \gamma_0 = 0)}\,\mathrm{d}x \qquad (8)$$

where $x_s/\delta_0^* = 700$ and $x_e/\delta_0^* = 1000$. Using this metric, it appears that the averaged ratio of the magnitudes is weakly dependent on the frequency of the perturbations (figure 12(*b*)). Furthermore, it appears that the relative magnitude of these perturbations is much more dependent on the momentum addition into the boundary layer through plasma actuation.

For small values of the velocity ratio, the level of damping is proportional to the velocity ratio (that is, $1 - B_u \propto \gamma_0$, figure 13(*a*)). However, as the magnitude of the velocity ratio increases, this linear approximation of the damping breaks down. For larger levels of plasma actuation, it appears that the relative damping of the TS wave is more closely related to the amount of momentum addition into the boundary layer by the plasma body force (figure 13(*b*)) and that the relative magnitude of the perturbations decreases exponentially with respect to D_c (that is, $B_u \propto \exp(-kD_c)$, where k is a constant).

5. Conclusion

The present bi-global stability analysis has examined how continuous momentum addition into a zero pressure gradient boundary layer through a plasma-based body force can be used to stabilize the TS path to transition. Two-dimensional

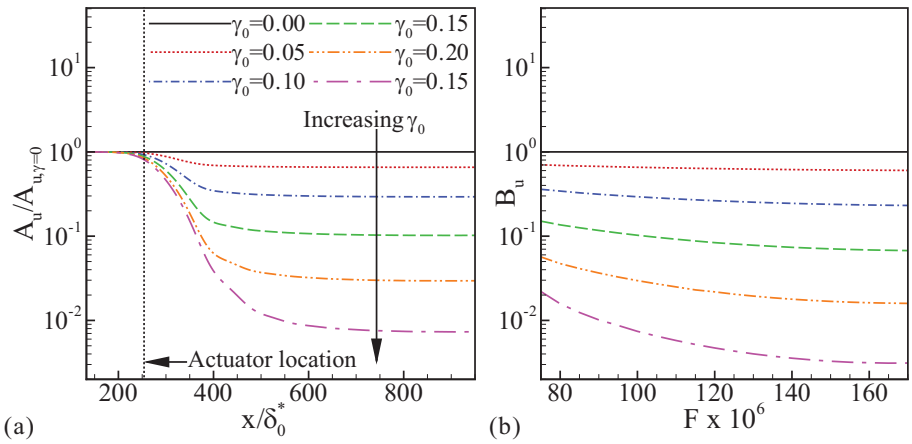

Figure 12. (*a*) A comparison of the ratio of the perturbation magnitudes for varying values of the velocity ratio γ_0 for the non-dimensional frequency $F \times 10^6 = 100$. (*b*) Average values of the velocity ratio along a length of the boundary layer downstream of the plasma actuation as a function of the non-dimensional frequency.

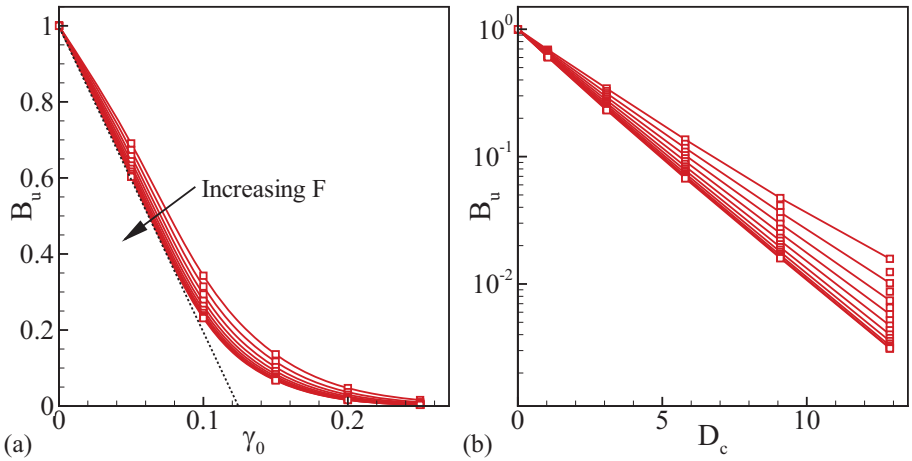

Figure 13. A comparison of the ratio of the perturbation magnitudes for varying non-dimensional frequencies $75 < F \times 10^6 < 175$ as a function of the (*a*) velocity ratio, and (*b*) proportional to the amount of momentum addition. The dashed lines indicate the (*a*) linear ($1 - B_u \propto \gamma_0$) decrease in the relative magnitudes of the perturbations.

boundary layer simulations are performed simulating the effects of a body force. The resulting boundary layer flows are characterized by the relevant flow effects. Parametric studies are performed by varying the frequency of the oncoming TS wave, as well as the magnitude of the body force injected into the flow.

By examining the local flow physics around and downstream of the momentum injection point, a number of different effects are seen to occur. There is a sudden stabilization of the flow around the actuator. Immediately downstream of the actuator, where the displacement boundary layer heights and shape factor are reduced, the TS perturbation is further stabilized, leading to a significant decrease in its magnitude. Sufficiently far downstream of the point of momentum addition, the effects of flow control become minimal, and the flow returns to its uncontrolled state.

Based on the parametric studies, the relative magnitude of the oncoming TS waves can be monotonically decreased as the body force injecting momentum into the flow is increased. The magnitude of the perturbation can be decreased by up to two orders of magnitude across a wide range of frequencies, though more modest reductions in perturbation magnitude are seen for smaller levels of plasma actuation. For smaller amounts of plasma actuation, the stabilization effects are proportional to the velocity ratio between the free-stream velocity and the induced velocity of the body force under quiescent conditions. For larger magnitudes of plasma actuations, the stabilization of the TS wave appears to be exponential with respect to the amount of momentum added to the boundary layer.

Future work in this topic should focus on examining the other paths to turbulence and any relevant receptivity mechanisms [4], as well as characterizing their behaviour at higher Reynolds numbers and in the presence of pressure gradients. While this study, along with other studies described in the literature, indicates that plasma actuators can be used to stabilize the TS transition path, the impact of using these actuators to control other instabilities, such as the growth of three-dimensional vortex streaks in boundary layers [23, 24], is still unknown. Furthermore, these actuators generate very localized changes in the boundary layer, which could lead to

the boundary layer becoming more receptive to free-stream perturbations [26], an issue that is yet to be examined for this particular type of actuator. However, if all of the available paths for the flow to transition to turbulence are stabilized over a sufficiently wide parametric space of boundary layer flows, then this manner of flow control could have a significant impact in reducing the turbulent skin friction experienced by air and ground vehicles.

Acknowledgments

The authors would like to thank Dr Miguel Visbal of the Air Force Research Laboratory for the use of the code FDL3DI. The first author would also like to thank the University of Florida's Graduate School Fellowship Award, which provided partial support for this study.

References

[1] Washburn A 2010 'NASA's current plans for ERA airframe technology' *48th AIAA Aerospace Sciences Meeting (Orlando, FL, 2010)*

[2] Salari K 2009 DOE's effort to reduce truck aerodynamic drag: joint experiments and computations lead to smart design *Technical Report* LLNL-PRES-411507, Lawrence Livermore National Laboratories

[3] Raghunathan R S, Kim H D and Setoguchi T 2002 Aerodynamics of high-speed railway train *Prog. Aerospace Sci.* **38** 469–514

[4] Morkovin M V 1969 On the many faces of transition *Viscous Drag Reduction* (New York: Plenum) pp 1–31

[5] Joslin R D 1998 Aircraft laminar flow control *Ann. Rev. Fluid Mech.* **30** 1–29

[6] Fransson J H M, Talamelli A, Brandt L and Cossu C 2006 Delaying transition to turbulence by a passive mechanism *Phys. Rev. Lett.* **96** 064501

[7] Albrecht T, Grundmann R, Mutschke G and Gunter G 2006 On the stability of the boundary layer subject to a wall-parallel Lorentz force *Phys. Fluids* **18** 098103

[8] Roth J R, Sherman D M and Wilkinson S P 1998 Boundary layer flow control with a one atmosphere uniform glow discharge surface plasma *46th AIAA Aerospace Sciences Meeting (Reno, NV, 1998) AIAA Paper* 1998-328

[9] Moreau E 2007 Airflow control by non-thermal plasma actuators *J. Phys. D: Appl. Phys.* **40** 605–36

[10] Grundmann S and Tropea C 2008 Delay of boundary-layer transition using plasma actuators *46th AIAA Aerospace Sciences Meeting (Reno, NV, 2008) AIAA Paper* AIAA 2008-1369

[11] Grundmann S and Tropea C 2009 Experimental damping of boundary-layer oscillations using DBD plasma actuators *Int. J. Heat Fluid Flow* **30** 394–402

[12] Duchmann A, Kurz A, Widmann A, Grundmann S and Tropea C 2012 Characterization of Tollmien–Schlichting wave damping by DBD plasma actuators using phase-locked PIV *50th AIAA Aerospace Sciences Meeting (Nashville, TN, 2012) AIAA Paper* AIAA-2012-0903

[13] Duchmann A, Grundmann S and Tropea C 2013 Delay of natural transition with dielectric barrier discharges *Exp. Fluids* **54** 1–12

[14] Riherd M and Roy S 2013 Local and bi-global stability analysis of a plasma actuated boundary layer *51st AIAA Aerospace Sciences Meeting (Grapevine, TX, 2013) AIAA Paper* AIAA-2013-0831

[15] Riherd M, Roy S and Balachandar S 2013 Local stability effects of plasma actuation on a zero pressure gradient boundary layer *Theor. Comput. Fluid Dyn.* doi:10.1007/s00162-013-0302-5

[16] Séraudie A, Vermeersch O and Arnal D 2011 DBD Plasma actuators effect on a 2D model laminar boundary layer. Transition delay under ionic wind effect *29th AIAA Applied Aerodynamics Conference (Honolulu, HI, 2011) AIAA Paper* AIAA 2011-3515

[17] Duchmann A, Simon B, Magin P, Tropea C and Grundmann S 2013 In-flight transition delay with DBD plasma actuators *51st AIAA Aerospace Sciences Meeting (Grapevine, TX, 2013) AIAA Paper* AIAA-2013-0901

[18] Rizzeta D P, Visbal M R and Morgan P E 2008 A high-order compact finite-difference scheme for large-eddy simulations of active flow control *Prog. Aerospace Sci.* **44** 397–426

[19] Singh K P and Roy S 2008 Force approximation for a plasma actuator operating in atmospheric air *J. Appl. Phys.* **103** 013305

[20] Durscher R and Roy S 2012 Evaluation of thrust measurement techniques for dielectric barrier discharge actuators *Exp. Fluids* **53** 1165–76

[21] Wazzan A R, Gazley C and Smith A M O 1979 Tollmien–Schlichting waves and transition: heated and adiabatic wedge flows with applications to bodies of revolution *Prog. Aerospace Sci.* **18** 351–92

[22] Squire H B 1933 On the stability of three-dimensional disturbances of viscous fluid between parallel walls *Proc. R. Soc. London* A **142** 621–38

[23] Ellingsen T and Palm E 1975 Stability of linear flow *Phys. Fluids* **18** 487–8

[24] Butler K M and Farrell B F 1992 Three-dimensional optimal perturbations in viscous shear flow *Phys. Fluids* A **4** 1637–50

[25] Jaffe N A, Okamura T T and Smith A M O 1970 Determination of spatial amplification factors and their application to predicting transition *AIAA J.* **8** 301–8

[26] Crouch J D 1992 Localized receptivity of boundary layers *Phys. Fluids* A **4** 1408–14